A Compact Mach-Zehnder Interferometer using Composite Plasmonic Waveguide for Ethanol Vapor Sensing

Souvik Ghosh and B. M. A. Rahman, *Fellow, IEEE*

***Abstract*— The Finite Element Method (FEM) has attracted a considerable interest in the past few decades for the analysis of a wide range of dielectric waveguides. This method can handle isotropic and anisotropic material properties and arbitrary shaped complex dielectric discontinuities more efficiently and accurately than any other methods. A modified H-field based full-vectorial finite element method is used for a rigorous analysis of a composite plasmonic waveguide (CPWG) as an efficient ethanol vapor sensor where a porous ZnO (P-ZnO) layer is used as low index material in between high index silicon and silver metal layer. Enhanced field confined into low index slot is utilized for ethanol vapor sensing which has many potential applications in food industries. It is reported here that, a high waveguide sensitivity over 0.7 per RIU could be realized with our proposed design depending on the porosity of the ZnO layer. For accurate detection of refractometric changes a compact Mach-Zehnder interferometer is designed where a maximum phase sensitivity of 0.30, 0.34, 0.38 and 0.40 is shown to be achieved for ~50% volume fraction of ethanol into porous ZnO layer with porosity, P = 30%, 40%, 50% and 60%, respectively. The complete investigation has been carried out at the well-known telecommunication wavelength 1550 nm and with our in-house, accurate full-vectorial FEM code.**

***Index Terms*— Finite element method (FEM), surface plasmon polariton (SPP), composite plasmonic waveguide, Mach-Zehnder Interferometer (MZI), Sensor.**

I. Introduction

MODERN industries use ethanol (CH_3CH_2OH) as one of the most important constituent. This highly flammable substance has a high impact on daily life, from chemical and pharmaceutical products to heavy automobile and fuel engineering. When ethanol vapor mixes with air, explosive fire can result if accidentally ignited. Only 3.5% ethanol vapor in air can causes explosion, this often termed as lower explosion limit. Besides, the upper explosion limit is 19% by volume of air [1]. Mishandling, leaking, spilling contamination failures can release the liquid ethanol which causes flammable vapor. This results environmental pollution and also severe health risks. Human body initially breaks ethanol into acetaldehyde which increases the risk factor of liver cirrhosis and cancer. Therefore, accurate and high sensitive sensing of ethanol vapor in industrial environment is crucial. Several gas sensing mechanisms, such as spectrometric sensing [2], electrochemical [3], [4], solid state semiconductor [5] and microcontroller based devices [6], have been reported and demonstrated in recent years. Besides, dielectric waveguide based interferometric and resonating structure**,** for breathing [7], H_2 [8] and CH_3CH_2OH [9] sensing is more convenient for its high sensitivity and compact lab-on-a-chip design. In this paper, we proposed a novel, compact ethanol vapor sensor based on hybrid plasmonic based horizontal slotted [10] waveguide which offers a high sensitivity along with nanometer scale footprint.

Integration of photonic devices and nano-electronics now became a challenge due to ingrained diffraction limit of electromagnetic energy supported by dielectric media. The surface plasmon polaritons (SPPs) can be one of the solutions to overcome this difficulty. Comparing other nano-scale waveguides, such as, high-index contrast silicon-on-insulator (SOI) nano-wires and photonic crystals (PCs), surface plasmon (SP) shows a true nano-scale light guiding [11], [12]. The light guiding characteristics of conventional dielectric waveguides and pure plasmonic waveguides are opposite in nature. A high-index contrast SOI nano-wire confines light in the high index region. A very low propagation loss and hundred nanometer scaled mode area are also key properties of these structures [13]. However, a pure metal plasmonic waveguide provides a sub-wavelength scale light guiding but with very high propagation loss [14] - [17]. This in turn demands an accurate engineering to design the plasmonic based waveguides to channelize the unique features of SPPs in the field of linear, non-linear photonic devices [18], [19] and sensing applications [20] - [21].

Surface Plasmon Polaritons (SPPs) are surface waves tightly confined at the interface between metal and dielectric media. At optical and near infra-red (IR) region, metal has negative dielectric constant whereas dielectrics show a positive value. This complimentary nature at the interface

This work was supported in part by City, University of London and in part by Erasmus Mundus AREAS+ Ph.D. fellowship program for Ph.D. and research funding.

The next few paragraphs should contain the authors' current affiliations, including current address and e-mail. For example, F. A. Author is with the National Institute of Standards and Technology, Boulder, CO 80305 USA (e-mail: author@ boulder.nist.gov).

The authors are with the Department of School of Mathematics, Computer Science and Engineering, City, University of London, London EC1V 0HB, U.K. (e-mail: souvik.ghosh.1@city.ac.uk; b.m.a.rahman@city.ac.uk).

excites electromagnetic surface wave that propagates until the field dies by material absorptions and scattering into surrounding media. The electromagnetic surface wave is a unique light-matter interaction that contains a coupled state of the electromagnetic wave to conductor's free electrons plasma oscillations. The SPPs are transverse magnetic (TM)-polarized in nature and evanescently confined in the direction of propagation. The SPPs can be excited either by electrons or photons with same frequency and momentum. In this piece of work the photons having telecommunication wavelength $\lambda = 1550\ nm$ is used for SPPs excitation. Analytical solution to characterize the modal properties of electromagnetic field generated on both side of the metal and its integration with dielectric waveguide mode for a complex structure is not easy. Numerical modelling of complex plasmonic structure offers possible solution for sub-wavelength plasmonic device design and its performance analysis. A full-vectorial **H**-field based FEM is used as a simulation tool for the device designs.

This report is organized as follows. In the 2nd section we summarize the modified mathematical steps of FV-FEM as well as the Lorentz-Lorenz formula to calculate equivalent refractive index of P-ZnO with ethanol vapor. The 3rd section describes the design of our proposed horizontal slotted composite plasmonic waveguide (CPWG). In the 4th section, the waveguide design parameters are optimized and evaluate its performance as an ethanol vapor sensor. The 5th section demonstrates the design and performance investigations of Mach-Zehnder interferometer using the P-ZnO based horizontal slotted CPWG. In section 6, the fabrication challenges are mentioned and finally, all findings are summarized in the *conclusive* part.

II. Theory

While designing of a pure [16], [17] and composite plasmonic waveguide (CPWG) [15], [18], [20], [22] an exact calculation of real and complex modal effective indices, dominating and non-dominating field components and hybridness of quasi-TM and quasi-TE modes are very important. Besides, in case of a sensor design, a rigorous analysis is also needed to calculate the confinement factors (Γ) of selective regions along with the modal effective index change due presence of a sensing medium. All aforementioned parameters could be found by solving the Maxwell's equations for the waveguide. In most cases the partial differential equations (PDEs) becomes complex, which are inadequate to solve by analytical or semi-analytical approach. Thus, a full vectorial numerically efficient finite element method (FV-FEM) could be used to determine the accurate modes of these waveguides. 2D FV-FEM uses for modal solution of the waveguide problem [23], [24] and 3D FV-FEM uses to determine the resonating nature of a structure [24], [25].

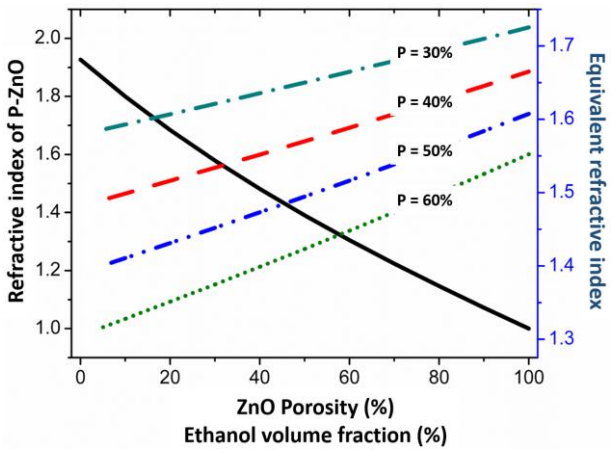

Fig. 1. Refractive index variation with porosity (P) and change of equivalent refractive index of P-ZnO with volume fraction (V) of condensed ethanol.

A. Full Vectorial Finite Element Method (FV-FEM)

In this report, we have used the **H** field based variational formulation. This method has a considerable advantage over other formulations, such as, **E** and mixed **E+H** field formulations, proposed in [26]. Here the **H** field components are continuous at the dielectric interfaces and this is true even when index contrast is high, such as metal-dielectric interface. Besides, the natural boundary condition associated with this formulation is a perfect electric wall (PEW). Thus, only necessary boundary condition (PEW and/or perfect magnetic wall (PMW)) needs to be imposed depending on the desired modes of the waveguides. One-fold and two-fold symmetrical advantage of the structure can be considered by proper application of PEW and PMW boundary conditions. Degeneration of different polarized modes can also be reduced with this mathematical trick. As a result, a better accuracy could be achieved with a much lower computational resource.

The variational formulation is based on Maxwell's two curl equations, so that, their Euler equations follow the Helmholtz's equation but do not necessarily satisfy the Maxwell's two divergence equations. This causes the presence of spurious modes all over the eigenvalue matrix along with the real modes. This formulation deficiency could be nullified by introducing a second part, so that the Euler equation of the modified functional $\boldsymbol{J_e}$ satisfy all four Maxwell's equations.

$$\begin{aligned} \boldsymbol{J_e} = \Big[\iint (\boldsymbol{\nabla}\times\boldsymbol{H})^* \cdot \hat{\epsilon_r}^{-1} (\boldsymbol{\nabla}\times\boldsymbol{H})\, dxdy \\ + p \iint (\boldsymbol{\nabla}\cdot\boldsymbol{H})^* (\nabla\cdot\boldsymbol{H})\, dxdy \Big] \\ - k_0^2 \Big[\iint \boldsymbol{H}^* \cdot \widehat{\mu_r}\, \boldsymbol{H}\, dxdy \Big] \end{aligned} \qquad (1)$$

Here the functional $\boldsymbol{J_e}$ represents the numerical errors due to domain discretization.

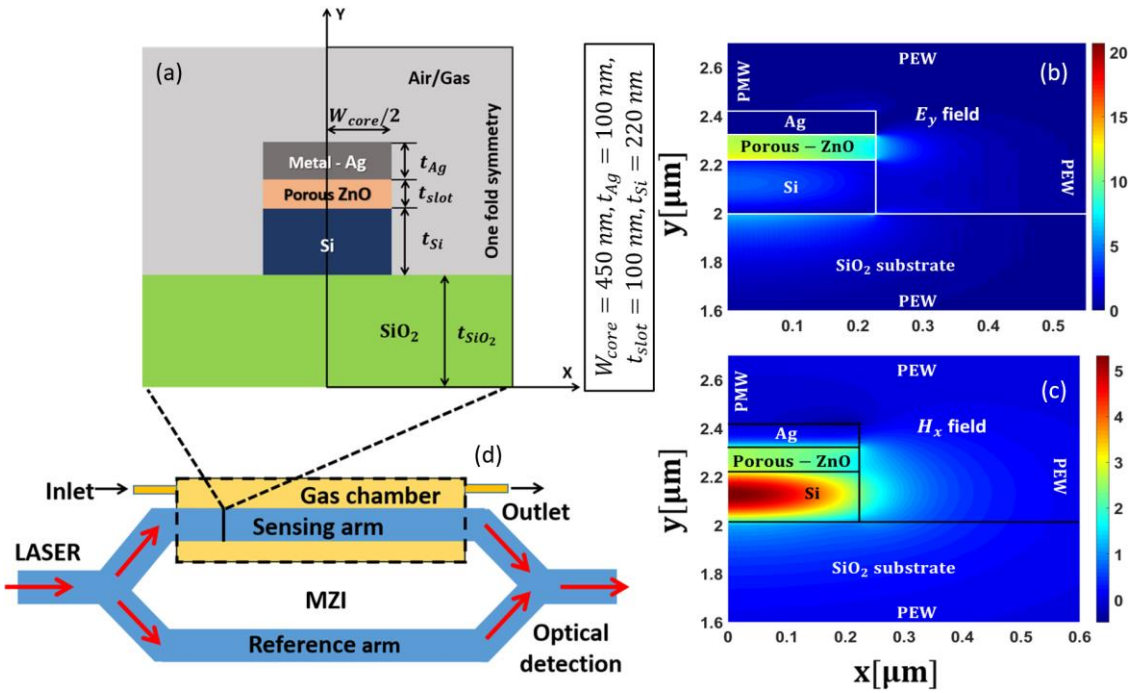

Fig. 2. Schematic diagram of a horizontal slotted CPWG and its simulated field distributions, (a) shows the geometrical cross-section of the proposed CPWG where P-ZnO is used as low index medium in between high index silicon (Si) and lossy metal (Ag). The black bordered region depicts the one folded computational domain. (b) and (c) are the E_y and H_x field distributions of fundamental quasi-TM (H_x^{11}) mode, respectively. One-fold symmetry is used during FEM simulations. (d) shows a MZI set-up where the proposed CPWG is used as the sensing and reference arm.

Rahman and Davies previously proposed the penalty function method [27] where a weighting factor p, shown in equation (1), was incorporated to externally balance the curl and divergence parts. As this penalty term is expected to almost equal to $1/n_{eff}^2$ of the waveguide, this has been very useful to give accurate modal solutions for waveguides with only positive dielectric constants. Instead of the penalty method reported earlier, we proposed here a more direct approach. This seems to be more effective for pure and composite plasmonic waveguide problems where the local material permittivity may have both positive and negative values. The plasmonic field variations occurs in small dimensions. To incorporate that the additional divergence integral is modified by considering the local permittivity rather than the global penalty parameter (p) used earlier. Here, during formation of global eigenvalue equation each discretized element's individual dielectric constant is considered inside the divergence part. The modified form of **H**-field based variational formulation can be written in the form

$$k_0^2 = \left(\frac{\omega}{c}\right)^2 = \frac{\iint (\boldsymbol{\nabla}\times\boldsymbol{H})^* \epsilon_r^{-1} (\boldsymbol{\nabla}\times\boldsymbol{H}) dxdy + \iint (\boldsymbol{\nabla}\cdot\boldsymbol{H})^* \epsilon_r^{-1} (\boldsymbol{\nabla}\cdot\boldsymbol{H}) dxdy}{\iint \boldsymbol{H}^* \cdot \mu_r \boldsymbol{H}\ dxdy} \quad (2)$$

Here k_0, ω, $\hat{\epsilon}$ and $\hat{\mu}$ are the wavenumber (k_0^2 represents the eigenvalue), angular frequency, relative permittivity and permeability tensor, respectively. The quasi-TE and TM modes can be obtained by post-processing the eigenvectors of specific eigenvalues.

Design and optimization of the vapor sensor needs a rigorous analysis of power confinement into selected slot region of the CPWG. The confinement factor of the horizontal slot can be defined by using the eigenvectors obtained from equation (2).

$$\Gamma_{slot} = \frac{\iint_{slot} Re(\boldsymbol{E}\times\boldsymbol{H}^*).\hat{z}\ dxdy}{\iint_{\infty} Re(\boldsymbol{E}\times\boldsymbol{H}^*).\hat{z}\ dxdy} \quad (3)$$

Where Re denotes the real part of complex electric ($\boldsymbol{E}$) and magnetic ($\boldsymbol{H}$) fields, respectively and * denotes the complex conjugate and integrations are carried out over the whole computation domain for denominator and only in the slot region for numerator.

B. Equivalent index of P-ZnO due to capillary condensation

Our proposed ethanol vapor sensor contains a horizontal layer of porous ZnO (P-ZnO) as a low index medium. P-ZnO has lower refractive index than a bulk ZnO, as the material pores are filled with air (n = 1). The equivalent refractive index has an inverse relation with the number of pores in unit volume, called *porosity* (P). Increased curved empty area due to porosity results the absorption and condensation of vapor or gas substances. Pore sizes ranging from 2 to 50 nm (mesoporous) of a P-ZnO layer possess the surface area around 1000 m^2/g [9]. When the porous layer is kept in contact with the measuring analyte the air (n = 1) filled voids are replaced by condensed analyte (n > 1). Depending on the different volume fraction of absorbed and condensed analyte,

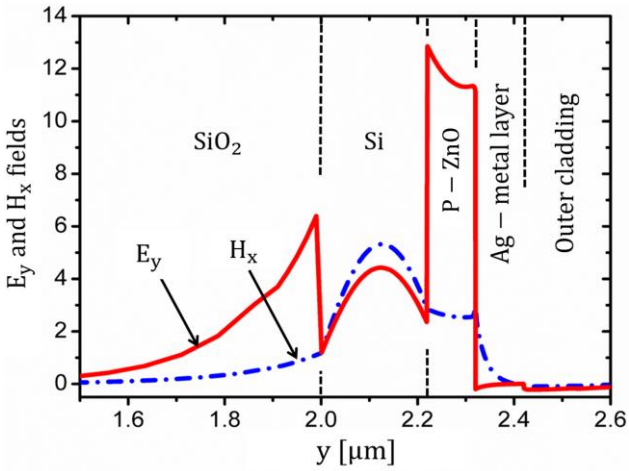

Fig. 3. Line plot of fundamental mode E_y and H_x field along the symmetry line (y-axis). The red solid curve shows E_y field enhancement in the low index horizontal slot region, effective for sensing applications. The blue dashed-dotted line shows light guidance by the dielectric Si core.

the effective refractive index as well as dielectric constant of P-ZnO changes.

To make our device efficient, different types of P-ZnO layer templates could be used, such as, porous flakes composed ZnO spheres [28], P-ZnO nanosheets [29] and nanoplates [30]. All these types of P-ZnO layers composites of nanometer scaled pores exploit ultrahigh pore density with great enhancement of surface-to-volume ratio. P-ZnO spheres, nanosheets and nanoplates are mesoporous with pore diameters ranging from 2 to 50 nm. The nanosheet contains average pore size of 39 nm [29]. Operating temperature is an important parameter for metal-oxide semiconductor based sensors. The P-ZnO sphere layer shows an enhanced selective response to 100 ppm ethanol at 280^0C. Similarly, a strong response in ethanol sensing can be observed around 400^0 to 450^0C for nanosheets and nanoplates [29], [30]. In terms of selectivity and response-recovery time, all three P-ZnO configurations show excellent selectivity and much lower response and recovery time (10 and 15 s, 7 and 19 s, 32 and 17 s) to ethanol vapor compared to methanol, acetone, chlorobenzene, methane at 280^0C [28], 400^0C [29] and ~450^0C [30] for 2, 200 and 100 ppm of ethanol, respectively. Use of these P-ZnO templates make the CPWG more stable and efficient for ethanol vapor sensing.

Various effective quantitative models, such as, Maxwell-Garnet theory, Bruggeman model and Lorentz-Lorenz model have been proposed to determine the equivalent permittivity of heterogeneous media [31]. In our work, we used the Lorentz-Lorenz model to determine the effective refractive index of P-ZnO and the equivalent refractive index (n_e) as

$$\frac{n_e^2-1}{n_e^2+2} = (1-P)\left(\frac{n_c^2-1}{n_c^2+2}\right) + (P-V)\left(\frac{n_a^2-1}{n_a^2+2}\right) + V\left(\frac{n_d^2-1}{n_d^2+2}\right) \quad (4)$$

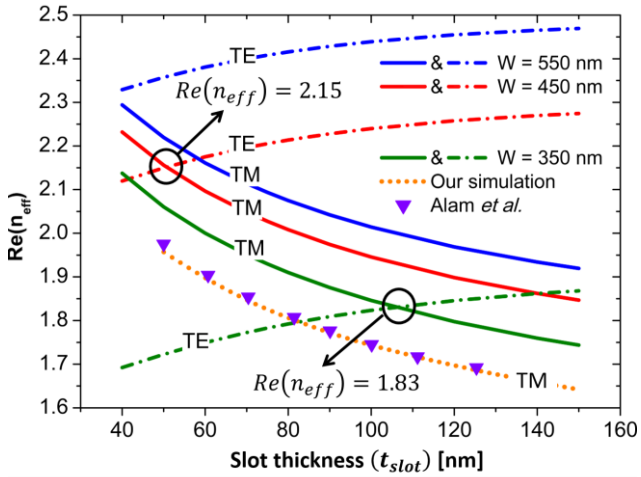

Fig. 4. Real effective index ($Re(n_{eff})$) variation with the slot thickness (t_{slot}). Fundamental quasi-TE (H_y^{11}) and TM (H_x^{11}) modal real effective indices with t_{slot} variations are shown by green, red and blue dashed-dotted and solid lines for three different core widths (W_{core}) 350, 450 and 550 nm, respectively. The orange dotted line denotes the $Re(n_{eff})$ of the quasi-TM mode simulated by our code for benchmarking with Alam *et al.*'s data [18] shown by purple triangular markers.

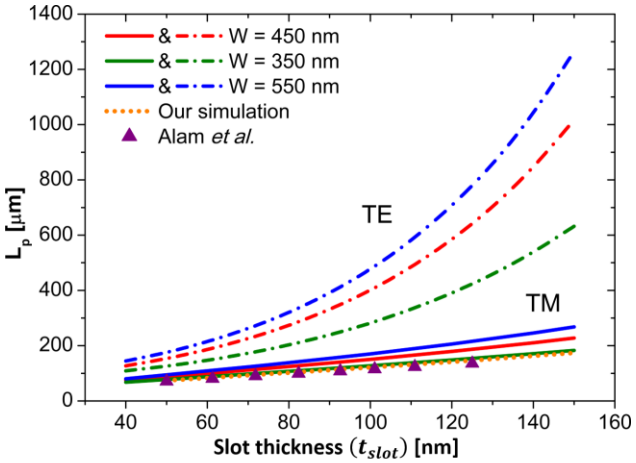

Fig. 5. Variation of the mode propagation length (L_p) with the t_{slot}. Quasi-TE modes (dashed-dotted lines) show higher L_p than quasi-TM mode (solid lines), shown by dashed-dotted and solid lines, respectively. 350, 450 and 550 nm W_{core} are represented by green, red and blue lines, respectively. The orange dotted line denotes the L_p of the quasi-TM mode simulated by our code for benchmarking with Alam *et al.*'s data [18] shown by purple triangular markers.

Here P is the ZnO layer porosity, V is the volume fraction of liquid after capillary condensation. n_a, n_c and n_d are the index of refraction of air (n_a = 1), homogenous (bulk ZnO) and dispersed medium (condensed vapour), respectively. We have considered the P-ZnO layer of porosity P = 30%, 40%, 50% and 60%. Corresponding refractive index (n_{P-ZnO}) variations and equivalent refractive index of P-ZnO due to different volume fraction of ethanol are presented in Fig. 1. As expected, with increased of porosity, n_{P-ZnO} decreases as shown by a solid black line. On the other hand, while the air pores are replaced by condensed ethanol the equivalent index of refraction increases. At room temperature (20^0C), the bulk ZnO refractive index is taken as 1.9267, derived from the

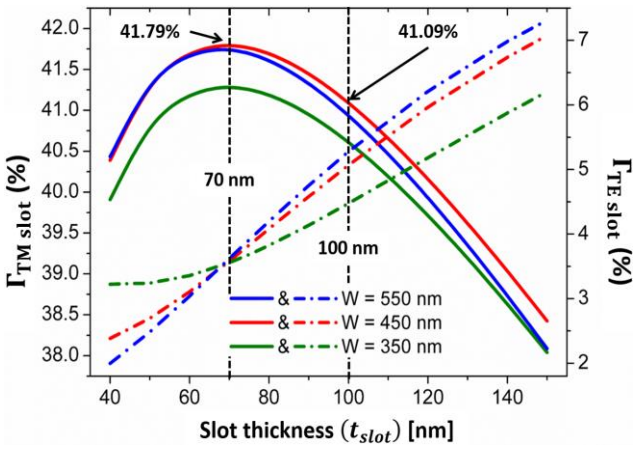

Fig. 6. Quasi-TM and TE slot confinement variations with t_{slot}. The TM slot confinement ($\Gamma_{TM\ slot}$) and TE slot confinement ($\Gamma_{TE\ slot}$) variations for three different W_{core} = 350, 450 and 550 nm are indicated by solid and dashed-dotted green, red and blue lines, respectively. W_{core}= 450 nm shows maximum $\Gamma_{TM\ slot}$ at t_{slot} = 70 nm.

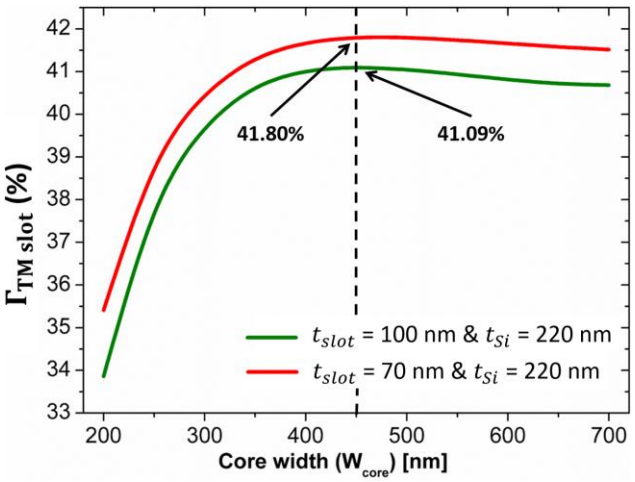

Fig. 7. The $\Gamma_{TM\ slot}$ variations with CPWG core width (W_{core}) for two different t_{slot}s. The red and green solid lines depict the same variations for t_{slot} = 70 nm and 100 nm, respectively. An over 41% power confinement is observed for W_{core} = 450 nm at t_{slot} = 70 nm and 100 nm.

dispersion formula in [32] and the condensed ethanol refractive index is derived by using the Sellmeier equation given in [33].

$$n^2(\lambda) - 1 = \frac{A_1\lambda^2}{\lambda^2 - B_1} + \frac{A_2\lambda^2}{\lambda^2 - B_2} \qquad (5)$$

Here $A_{1,2}$ and $B_{1,2}$ denotes the material property parameters and absorption wavelengths. The constant values used for mathematical analysis are, $A_1 = 0.83189$, $A_2 = -0.15582$, $B_1 = 0.00930\ \mu m^{-2}$ and $B_2 = -49.45200\ \mu m^{-2}$.

III. Horizontal Slotted Composite Plasmonic Waveguide

Plasmonic waveguides are very useful for nano-dimensioned photonic sensing devices. In pure plasmonic and CPWG, enhanced sub-diffraction limited light confinement on the metal-dielectric interface make this structure very attractive for local surface and bulk bio-chemical and gas sensing. The presence of lossy metal the bounded SPP modes can only be guided over a small distance. To utilize the advantages of localized plasmonic fields along with short mode propagation length (L_p) the metal layer is integrated with other dielectric materials. The propagation length (L_p) is defined by $L_p = 1/2\alpha = \lambda/4\pi\ Im(n_{eff})$, where α denotes the attenuation constant and $Im(n_{eff})$ denotes the imaginary part of effective index. Metal dielectric composite structure helps the plasmonic modes to propagate over a comparative longer distance. Thus, with proper engineering a composite plasmonic waveguide (CPWG) can be designed, which can be useful for local bio-chemical and gas sensing.

The schematic diagram of our proposed horizontal slotted CPWG is shown in Fig. 2(a). The waveguide consists of composite materials, such as lossy metal (Ag), porous ZnO (P-ZnO), silicon (Si) and silica (SiO_2). A horizontal slot waveguide can be formed by depositing a nano-scaled thick (t_{Ag}) silver layer on top of a P-ZnO, which is used as a low index slot region in between the metal and high index Si. The refractive indices considered for simulations are, $n_{Ag} = 0.13880 + j11.310$ [34], $n_{Si} = 3.4757$ [35], $n_{SiO2} = 1.4440$. The necessary boundary condition of electromagnetic field demands a continuity of normal component of electric flux density ($\boldsymbol{D}$) at the interface boundaries that results a high E_y field discontinuity at those interfaces. These field characteristics make this waveguide very attractive for integrated sensing device due to strong light matter interaction in the slot region. Here ethanol vapor is used as a sensing medium. Due to capillary condensation ethanol vapor molecules are absorbed by the ZnO pores and condensed as liquid ethanol. Thus, depending on percentage of absorbed ethanol vapor the refractive index of P-ZnO layer changes. The relation between equivalent refractive index of P-ZnO and volume fraction of ethanol already has been discussed in Section 2.3. These refractometric change can easily be detectable by an accurate measurement of waveguide's real part of effective index change, $\Delta Re(n_{eff})$ of the quasi-TE and TM modes.

An efficient **H**-field based FEM code is used to simulate the CPWG. In Fig. 2(a), only the right hand side section bordered by black line have been considered for simulation as we have exploited the available symmetry of the structure. To obtain an accurate solution and field continuity of CPWG, the boundary conditions are applied along the symmetry line. In this structure, a perfect magnetic wall (PMW), $\hat{n}\times\boldsymbol{H} = 0$ is applied along the symmetry line (along y-axis) as the H_x and E_y fields of fundamental mode have even symmetry along the y-axis. Figures 2(b) and (c) depict the E_y and H_x field contours of fundamental H_x^{11} mode. The 1D-line plot of E_y and H_x fields of fundamental H_x^{11} mode is shown in Fig. 3. The E_y field by the red solid line indicates a sharp field enhancement into low index horizontal slot region. The H_x field is denoted by blue

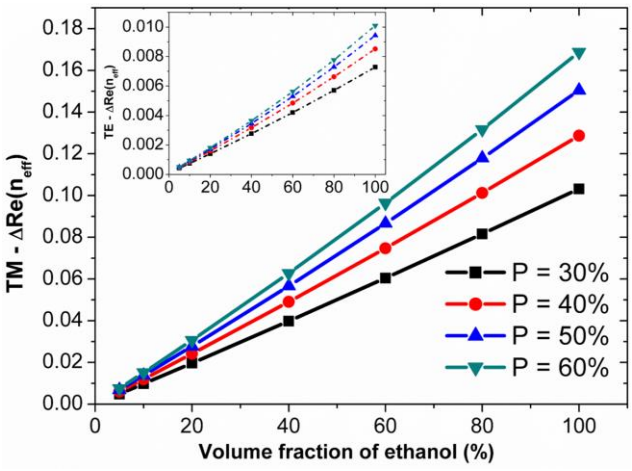

Fig. 8. Quasi-TM effective index change ($\Delta Re(n_{eff})$) against volume fraction of ethanol into P-ZnO layer. Quasi-TE changes are shown as an inset. The black, red, blue and cyan solid and dashed lines in main and inset plot depict the TM and TE modal $\Delta Re(n_{eff})$ changes due to different volume fraction of ethanol into 30%, 40%, 50% and 60% porous ZnO layers, respectively.

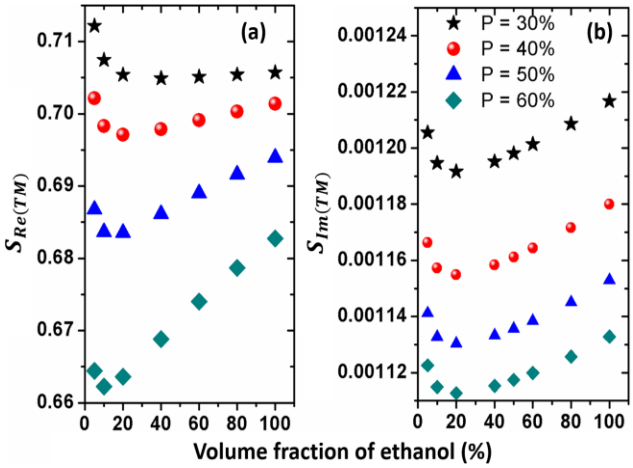

Fig. 9. (a) and (b) represent the CPWG quasi-TM real effective index sensitivity ($S_{Re(TM)}$) and normalized attenuation sensitivity ($S_{Im(TM)}$) variations with volume fraction of ethanol into horizontal slotted P-ZnO layer, respectively. The black star, red ball, blue triangle and cyan diamond markers on both figures illustrate the sensitivity variation with absorbed ethanol vapor into P-ZnO slot having porosity, P = 30%, 40%, 50% and 60%, respectively.

dashed-dotted line which shows light guidance by the high index Si core. To obtain an explicit sensor design a rigorous investigation is needed to estimate the optimized waveguide parameters, dominant, non-dominant field distributions and power confinement into different waveguide regions due to refractometric changes into slot area. For simplicity, we fixed the Si nano-wire and Ag metal thickness as 220 nm and 100 nm, respectively. The rest of device geometries, such as, waveguide core width (W_{core}) and slot thickness are (t_{slot}) are optimized for best performance. Throughout the simulation process, only half of the waveguide is discretized with 1,280,000 triangular mesh elements. Mesh distribution is also an important part for plasmonic waveguides. As the metal surface possess a sub-wavelength field confinement into nano-scaled region, a sufficient dense mesh distribution is required in the thin metal area for accurate solutions. The maximum element size used around the metallic area is better than 0.2 nm.

IV. Design Parameters Optimization and Performance Evaluation

Figures 4 and 5 show variation of the real part of the effective index, $Re(n_{eff})$ and modal propagation length L_p against the horizontal slot thickness t_{slot}, respectively. To benchmark our in-house code developed over 30 years, we have also simulated a SOI based horizontal slotted hybrid-plasmonic waveguide proposed by Alam *et al.* [18]. We have considered the same waveguide dimensions ($W_{core} = 350\ nm, t_{Ag} = 200\ nm, t_{Si} = 200\ nm$ and $t_{substrate} = 2.0\ \mu m$) and same material refractive indices for our simulations. Our simulated $Re(n_{eff})$ and L_p data are shown by the orange dotted lines in Figs. 4 and 5. Our results matches excellently with the published results (purple triangles) reported in [18] where they have used a commercial software for simulations.

In this study, we have taken three different widths 350 nm, 450 nm and 550 nm shown by green, red and blue lines, respectively. Corresponding $Re(n_{eff})$ and L_p variations of fundamental quasi-TE and TM mode are shown by the dashed-dotted and solid lines, respectively. As t_{slot} increases the $Re(n_{eff})$ decreases gradually for fundamental quasi-TM mode but increases for fundamental quasi-TE mode, respectively. It can be observed that for W_{core} = 350 nm and 450 nm modal degeneracy occurs at t_{slot} = 108 nm and 48 nm, respectively when effective indices of the quasi-TE and quasi-TM modes became equal. Modal degeneracy points are encircled by black line and corresponding $Re(n_{eff})$ values are also given in Fig. 4. Here for CPWG, the effective dominant mode for sensing is the quasi-TM supermode where a surface plasmonic mode is coupled with dielectric mode into low index slot region. It can also be noted from Fig. 4 that for a fixed t_{slot} the $Re(n_{eff})$ also decreases with W_{core}. The L_p variations with t_{slot} in Fig. 5 show a rapid increment for quasi-TE as here the field is mostly confined and also guided by the low-loss dielectric regions but the quasi-TM mode shows a comparative slow increment with thickness of P-ZnO dielectric material into slot as here the field profile is dominated by the SPPs generated by the lossy metal-dielectric interface.

Figures 6 and 7 show the quasi-TE and TM confinements with t_{slot} and W_{core}, respectively. The TE and TM slot confinements ($\Gamma_{TM\ slot}$ and $\Gamma_{TE\ slot}$) with t_{slot} show an interesting feature. For three fixed W_{core}, the $\Gamma_{TM\ slot}$ increases with t_{slot}, reaches maximum 41.79% at t_{slot} = 70 nm and then decreases gradually with further increment. It can also be noticed that the CPWG with W_{core} = 450 nm, shown by the red solid line, confines higher electromagnetic energy than other two core widths (550 and 350 nm), shown by blue and green solid lines, respectively. The $\Gamma_{TE\ slot}$ for all three W_{core} increase with increase of slot thickness shown by the dashed-

dotted lines. But these values are considerably lower than the TM mode confinement. These curves intersect each other at $t_{slot} = 68\,nm$ and exhibits only around 3.56% power confinement. As we are designing a plasmonic sensor, the slot confinement due to SPP and dielectric supermode is our most concern. As a result, we focused only on $\Gamma_{TM\,slot}$ variation and the maximum confinement is obtained for optimized slot thickness, t_{slot} = 70 nm. Further optimization of W_{core} for 70 nm and 100 nm slot height has been carried out and the result is presented in Fig. 7. Here, the red and green solid lines represent the $\Gamma_{TM\,slot}$ variations with W_{core} for two fixed t_{slot} = 70 nm and 100 nm, respectively. As W_{core} increases the $\Gamma_{TM\,slot}$ grows and confines maximum 41.80% and 41.09% TM field into 70 and 100 nm slot, respectively at W_{core}= 450 nm. Thus, the optimized CPWG core width can be taken as 450 nm. From the plots in Figs. 6 and 7 it can be seen that a 100 nm slot confines 41.09% TM field. As there was not much difference in $\Gamma_{TM\,slot}$ for t_{slot} = 70 nm and 100 nm and a few nm extra thickness may be convenient to accommodate more number of pores in mesoporous ZnO layer, we have finally considered slot thickness as 100 nm. Throughout the optimization process, the Si nano-wire and Ag thickness are kept fixed at t_{Si} = 220 nm and t_{Ag} = 100 nm, respectively but if desired these can also be optimized. Hence all the optimized CPWG parameters can be listed as, W_{core} = 450 nm, t_{slot} = 100 nm, t_{Si} = 220 nm and t_{Ag} = 100 nm for 40% ZnO porosity.

Next, we analyzed the CPWG performance with the presence of ethanol vapor. Absorption of different percent ethanol vapor changes the equivalent refractive index of P-ZnO with the help of capillary condensation. The equivalent refractive index depending on the volume fraction of ethanol was calculated by using Lorentz-Lorenz formulation, given in equation (3) and also shown in Fig. 1. The quasi-TM and TE real effective index difference ($\Delta Re(n_{eff})$) of the CPWG with volume fraction of ethanol for different P-ZnO are depicted in Fig. 8. The black, red, blue and green solid lines indicate the TM-$\Delta Re(n_{eff})$ variation whereas the dashed lines show the same for TE-$\Delta Re(n_{eff})$, respectively. Although we optimized our structure for P = 40%, but for a comparative study we also considered three other different ZnO porosity, P = 30%, 50% and 60%. As the volume fraction of ethanol into P-ZnO layer increases both the TM-$\Delta Re(n_{eff})$ and TE-$\Delta Re(n_{eff})$ increase. 5% to 100% absorbance of ethanol vapor makes a 0.31% to 6.62% TM-$\Delta Re(n_{eff})$ change for P = 40% whereas a much lower value only 0.02% to 0.38% TE-$\Delta Re(n_{eff})$ change is observed for same porosity, shown by red solid and dashed lines in Fig. 8(a) main and inset, respectively. For other ZnO porosity, such as P = 30%, the TM-$\Delta Re(n_{eff})$ shows a change from 0.24% to 5.13% for 5% to 100% ethanol vapor absorption. On the other hand, P-ZnO with porosity P = 60%, a higher TM-$\Delta Re(n_{eff})$ change from 0.41% to 9.24% can be observed for the same volume fraction of ethanol. Thus, higher porosity shows better quasi-TM effective index change. We have also studied the CPWG's quasi-TM modal sensitivity with the volume fraction of absorbed ethanol. The black star, red ball, blue triangle and

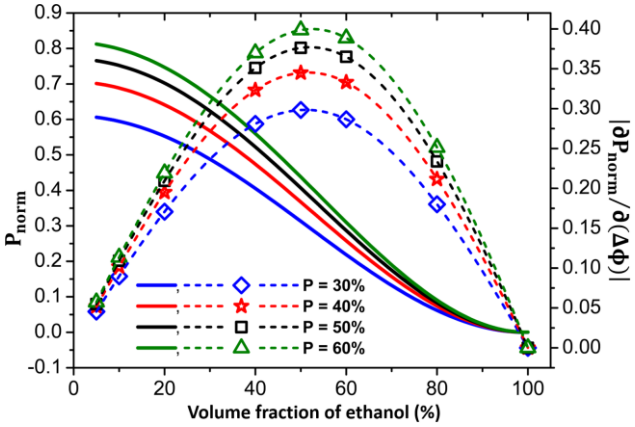

Fig. 10. MZI normalized output power (P_{norm}) and phase sensitivity $|\partial P_{norm}/\partial(\Delta\phi)|$ variations against volume fraction of ethanol into P-ZnO. Blue diamond, red star, black square and green triangle markers with dashed lines denote sinusoidal $|\partial P_{norm}/\partial(\Delta\phi)|$ variations for different porosity, P = 30%, 40%, 50% and 60%, respectively. The solid blue, red, black and green lines indicate cosine natured P_{norm} variations for all four P-ZnO layers.

cyan diamond markers in Figs. 9(a) and (b) show the real effective index refractometric sensitivity ($S_{Re(TM)} = \Delta Re(n_{eff})/\Delta n_{slot}$) and normalized waveguide attenuation sensitivity ($S_{Im(TM)} = \Delta Im(n_{eff})/\Delta n_{slot}$) of the fundamental quasi-TM mode for P-ZnO layer having porosity, P = 30%, 40%, 50% and 60%, respectively. For each P-ZnO layer, the $S_{Re(TM)}$ and $S_{Im(TM)}$ initially decrease up to ~15% ethanol absorption and then increases as the volume fraction of ethanol increase. Figs. 9(a) and (b) also indicate that a P-ZnO layer with lower porosity (P = 30%) shows higher $S_{Re(TM)}$ and $S_{Im(TM)}$ (black stars) than a P-ZnO layer with double porosity (P = 60%), shown by cyan diamonds. In the case of waveguide based sensor design, the $S_{Re(TM)}$ is more important than $S_{Im(TM)}$. The result in Fig. 9(a) shows a much higher $S_{Re(TM)}$ ($\approx$ 0.71 per RIU) can be achieved with our proposed CPWG structure. Besides, Fig. 9(b) reveals that the normalized attenuation of the CPWG is less sensitive to slot refractometric changes. This indicates a very small loss change due to different volume fraction of ethanol into P-ZnO.

Fig. 8 demonstrates that a P-ZnO layer with high porosity is good for detection of refractometric changes due to ethanol absorption whereas, in terms of waveguide sensitivity (Fig. 9(a) and (b)), a P-ZnO layer with lower porosity shows higher effectiveness. This contradictory result can be explained with the help of Fig. 1. Equivalent refractive index variation of 60% P-ZnO layer with volume fraction of ethanol is much stepper than 30% P-ZnO layer. This makes the CPWG $S_{Re(TM)}$ and $S_{Im(TM)}$ higher for a P-ZnO layer having lower porosity.

V. CPWG INCORPORATED MACH-ZEHNDER INTERFEROMETER (MZI)

To determine the effective index change during ethanol vapor sensing process, a Mach-Zehnder interferometer (MZI) could be used as a transducer device. The MZI schematic is shown in Fig. 2(d) where two parallel arms are connected with

one input and one output by using well designed 3 dB optical splitters. Our proposed CPWG is incorporated in MZI arms. One arm is called *sensing arm* where the integrated CPWG is passed through ethanol vapor filled gas chamber to measure the volume fraction of ethanol and while another CPWG is used in *reference arm*. The insertion phase difference ($\Delta\phi$) between sensing and reference arm could be measured from the effective index change $\Delta Re(n_{eff})$ due different volume fraction of ethanol, as

$$\Delta\phi = \frac{2\pi}{\lambda} \cdot \Delta Re\left(n_{eff}\right) \cdot L \qquad (6)$$

Here, L denotes the CPWG incorporated MZI arm length. A π phase difference between sensing and reference arm makes a destructive interference that results a zero MZI output. The CPWG incorporated MZI arm length are calculated as 7.51, 6.02, 5.15 and 4.59 μm for each type of P-ZnO layer having porosity, P = 30%, 40%, 50% and 60%, respectively. Thus, higher porosity gives higher Δn_{eff} which results shorter L. Same optimized design parameters (W_{core} = 450 nm, t_{slot} = 100 nm, t_{Si} = 220 nm and t_{Ag} = 100 nm) are used for CPWG structure. We have also studied the corresponding propagation loss arises due to different CPWG length and a much low loss value around 0.2 dB has been calculated for each of the CPWG with their aforementioned lengths. More precisely, with and without ethanol vapor the waveguide loss change in CPWG incorporated MZI arms are 0.045 dB for P = 30%, 40% and 50% and 0.047 dB for P = 60%, respectively. Although, CPWG has high loss compared to conventional dielectric waveguide however, the small footprint of CPWG provides a much lower propagation loss.

The normalized output power (P_{norm}) of CPWG incorporated MZI carries the $\Delta Re(n_{eff})$ information in terms of $\Delta\phi$, is given by

$$P_{norm} = \frac{P_{out}}{P_{in}} = \frac{1}{2}\, e^{-2\alpha L}\,(1 + \cos\Delta\phi) \qquad (7)$$

Here, α is the attenuation constant of the waveguide. All the MZI powers are normalized with respect to the input power P_{in}. The normalized output power (P_{norm}) have a cosine variation with phase difference. Often it is assumed that the attenuation (α) is same for both MZI arms with identical waveguides. however, for sensing purpose, the reference and the sensing arm waveguides may have different attenuations, $\alpha_{ref} = \alpha$ and $\alpha_{sen} = \alpha \pm \Delta\alpha_{sen}$, respectively. The sensing waveguide attenuation is modified by a small change $\Delta\alpha_{sen}$ due to different absorption levels of ethanol vapor. It can be shown that, this modifies the normalized MZI output power as [36]

$$P_{norm} = \frac{1}{2}\, e^{-2\alpha L}\, e^{-\Delta\alpha_{sen}L}\, \cosh(\Delta\alpha_{sen}L)\; (1 + F\cos\Delta\phi) \qquad (8)$$

Here, the F is identified as interferometric fringe contrast, which depends on $\Delta\alpha_{sen}$ as, $F = 1/\cosh(\Delta\alpha_{sen}\, L)$. Additionally, a section of the equation (8) could be termed as *power fraction* (PF = $e^{-\Delta\alpha_{sen}L}\cosh(\Delta\alpha_{sen}L)$) which indicates the increase or decrease in power compared to the reference arm waveguide. P_{norm} is only measurable parameter that changes with the phase difference in between sensing and reference arms. Thus, a phase sensitivity of the device is an important parameter which can be defined by

$$\frac{\partial P_{norm}}{\partial(\Delta\phi)} = -\frac{1}{2} e^{-(2\alpha+\Delta\alpha_{sen})L} \cosh(\Delta\alpha_{sen}L)\, F \sin(\Delta\phi) \qquad (9)$$

The equation shows that the maximum phase sensitivity occurs for $\Delta\phi = \frac{\pi}{2}$. Figure 10 shows the normalized power (P_{norm}) and absolute value of phase sensitivity $|\,\partial P_{norm}/\partial(\Delta\phi)\,|$ variations of proposed CPWG incorporated MZI against ethanol volume fraction for different P-ZnO. Different markers with dashed lines and solid lines are used to indicate the $|\partial P_{norm}/\partial(\Delta\phi)|$ and P_{norm} variations. Blue, red, black and green solid lines indicate cosine variations of P_{norm} with volume fraction of ethanol into P-ZnO of porosity, P = 30%, 40%, 50% and 60%, respectively. This figure depicts that 100% ethanol vapor absorption in sensing arm makes a π phase difference with zero MZI output and a 5% (considered as minimum) volume fraction of ethanol imposes a minimum phase difference with maximum 60%, 70%, 76% and 81% light output for 30%, 40%, 50% and 60% P-ZnO, respectively. Higher porosity provides better light output. The $\Delta\phi$ shows an *almost* linear relationship with ethanol volume fraction. Blue diamond, red star, black square and green triangles with dashed lines depicts a sinusoidal variation of $|\partial P_{norm}/\partial(\Delta\phi)|$ for four different P-ZnO layers. Lower porosity (P = 30%) shows lower phase sensitivity, shown by the blue dashed line with diamond marker, whereas, the green dashed line with triangular marker shows a much better phase sensitivity for porosity, P = 60%. Considering device sensitivity, all ZnO layers with different porosity, P = 30%, 40%, 50% and 60% exhibit maximum phase sensitivities of 0.30, 0.34, 0.38 and 0.40 when 51.57%, 52.05%, 52.59% and 53.16% of the ZnO pores are filled by the condensed ethanol, respectively when an exact $\frac{\pi}{2}$ phase difference is obtained in between sensing and reference arms. A MZI with lossless identical waveguide exhibits almost same phase sensitivities for all P-ZnO layers. In this CPWG incorporated MZI, the balance between both arms break down due to different attenuations ($\alpha_{ref} \neq \alpha_{sen}$). To make an error-free MZI design, the device attenuation should be controlled in a way such that it does not reduce the interferometer balance. In our study, for all volume fractions of ethanol into 30%, 40%, 50% and 60% P-ZnO the fringe contrast (F) was ~0.99 and the power fraction (PF) was ~0.96. This ($F \approx$ PF ≈ 1) indicates that in this case the extra attenuation change in the sensing waveguide is very small to cause any noticeable effect in the CPWG incorporated MZI performance.

VI. Fabrication Challenges

The Si nano-wire could be easily realized by modern CMOS fabrication technologies. Lithography masking and

then controlled dry-etching of a commercially available silicon-on-insulator (SOI) wafer can be used to fabricate a finite width (W_{core}) fixed height (t_{Si} = 220 nm) Si nano-wire. Although different chemical strategies are available to grow P-ZnO, such as, sol-gel, thermal decomposition, laser ablation that uses a high temperature, a low temperature synthesis mechanism using precipitation method [9], [37] could be useful to grow a controlled thickness (t_{slot}) P-ZnO nano layer on Si. A ZnO nanocrystal layer can be formed by using additive materials with the pure Zn based solution and then deposit it onto Si nano-wire by the process of uniform precipitation method. To achieved mesoporous crystallized ZnO, the additive materials residue need to be evaporate by heat treatment. The pore dimensions and quality could be controlled by the additive material concentration, molecular size and operating temperature. Here we considered a mesoporous ZnO layer with pore sizes between 2 to 50 nm.

VII. Conclusions

In summary, a SOI based composite plasmonic waveguide (CPWG) is investigated where a porous ZnO layer is used as a horizontal slot for ethanol vapor sensing. A **H**-field based FEM is used for analyses. These simulations revel that the CPWG can guide a hybrid plasmonic supermode, comprises of SPPs and dielectric mode, over a sufficiently long distance. A nano-scale (450 nm × 100 nm) field confinement is obtained and then exploited to detect the refractometric changes due to ethanol vapor absorption and condensation. All the design parameters are optimized for the best possible result. The proposed CPWG shows a high waveguide sensitivity 0.7 per RIU for 40% porous ZnO layer as horizontal slot. This CPWG is used in both arms of a compact Mach-Zehnder interferometer (MZI) to measure the refractive index change. The MZI output power with different volume fraction of absorbed ethanol into P-ZnO for various porosity also have been analyzed and reported. Different phase sensitivities (0.30, 0.34, 0.38 and 0.40) for the proposed sensors are observed for 51.57%, 52.05%, 52.59% and 53.16% ethanol condensation into horizontally slotted ZnO layer with porosity, P = 30%, 40%, 50% and 60%, respectively.

Thus, numerically simulated investigation successfully serves a demonstration of label free ethanol vapor sensor using a coupled SPP and dielectric field confined in a low index nano-scale horizontal slot. In practice, due to simplicity this compact CPWG can be easily achieved with modern fabrication technologies and advanced surface chemistry. Based on the reported results, the present work shows a potential application of this composite plasmonic waveguide in environmental gas and vapor sensing mechanism.

References

[1] Gas L. "Lower and upper explosive limits for flammable gases and vapors (LEL/UEL)," Matheson Gas Products, 2013.

[2] A. Kuze, H. Suto, M. Nakajima, and T. Hamazaki, "Thermal and near infrared sensor for carbon observation fourier-transform spectrometer on the greenhouse gases observing satellite for greenhouse gases monitoring," *Appl. Opt.*, vol. 48, no. 35, pp. 6716 – 6733, 2009.

[3] J. Chen, L. Xu, W. Li, and X. Gou, "$\alpha - Fe_2O_3$ nanotubes in gas sensor and lithium-ion battery applications," *Adv. Mater.*, vol. 17, no. 5, Mar. 2005.

[4] T. Zang, M. B. Nix, B. Y. Yoo, M. A. Deshusses, and N. V. Myung., "Electrochemically functionalized single-walled carbon nanotube gas sensor," *Electroanalysis*, vol. 18, no. 12, pp. 1153 – 1158, May. 2006.

[5] D. Gibson and C. MacGregor, "A novel solid state non-dispersive infrared CO_2 gas sensor compatible with wireless and portable deployment," *Sensors*, vol. 13, no. 6, pp. 7079 – 7103, 2013.

[6] S. Abraham and X. Li, "A cost-effective wireless sensor network system for indoor air quality monitoring applications," *Procedia Comput. Sci.*, vol. 34, no. 0, pp. 165 – 171, 2014.

[7] F. C. Favero, J. Villatoro, and V. Pruneri, "Microstructured optical fiber interferometric breathing sensor," *J. Biomed. Opt.*, vol. 17, no. 3, pp. 037006 – 1 – 037006 – 5, Mar. 2012.

[8] N. A. Yebo D. Taillaert, J. Roels, D. Lahem, M. Debliquy, D. van Thourhout, and R. Baets, "Silicon-on-insulator (SOI) ring resonator-based integrated optical hydrogen sensor," *IEEE Photon. Techno. Lett.*, vol. 21, no. 14, pp. 960 – 962, 2009.

[9] N. A. Yebo, P. Lommens, Z. Hens, and R. Baets, "An integrated optic ethanol vapor sensor based on a silicon-on-insulator microring resonator coated with a porous ZnO film," *Opt. Express*, vol. 18, no. 11, pp. 11859-11866, 2010.

[10] V. R. Almeida, Q. Xu, C. A. Barrios, and M. Lipson, "Guiding and confining light in void nanostructure," *Opt. Lett*., vol. 29, no. 11, pp. 1209 – 1211, Jun. 2004.

[11] S. A. Maier, *Plasmonics: Fundamentals and applications*, Springer, 2007.

[12] R. F. Oulton, V. J. Sorger, D. A. Genov, D. F. P. Pile, and X. Zhang, "A hybrid plasmonic waveguide for subwavelength confinement and long-range propagation," *Nature Photon.*, vol. 2, pp. 496 – 500, 2008.

[13] N. Kejalakshmy, A. Agrawal, Y. Aden, D. M. H. Leung, B. M. A. Rahman, and K. T. V. Grattan, "Characterization of silicon nanowire by use of full-vectorial finite element method," *Appl. Opt.*, vol. 49, no. 16, pp. 3173-3181, 2010.

[14] G. Veronis and S. Fan, "Guided subwavelength plasmonic mode supported by a slot in a thin metal film," *Opt. Lett.*, vol. 30, no. 24, pp. 3359 – 3361, 2005.

[15] A. V. Krasavin and A. V. Zayats, "Silicon-based plasmonic waveguides," *Opt. Express.*, vol. 18, no. 11, pp. 11791-11799, May. 2010.

[16] P. Berini, "Plasmon-polariton waves guided by thin lossy metal films of finite width: Bound modes of symmetric structures," *Phys. Rev. B.*, vol. 61, no. 15, pp. 10484 – 10503, Apr. 2000.

[17] P. Berini, "Plasmon-polariton waves guided by thin lossy metal films of finite width: Bound modes of asymmetric structures," *Phys. Rev. B.*, vol. 63, no. 12, pp. 125417-1 – 125417-15, Mar. 2001.

[18] M. Alam, J. S. Aitchsion, and M. Mojahedi, "Compact hybrid TM-pass polarizer for silicon-on-insulator platform," *Appl. Opt.*, vol. 50, no. 15, pp.2294 – 2298, 2011.

[19] F. F. Lu, T. Li, J. Xu, Z. D. Xie, L. Li, S. N. Zhu, and Y. Y. Zhu., "Surface plasmon polariton enhanced by optical parametric amplification in nonlinear hybrid waveguide," *Opt. Express*, vol. 19, no. 4, pp. 2858 – 2865, Jan. 2011.

[20] M. Z. Alam, F. Bahrami, J. S. Aitchison, and M. Mojahedi, "Analysis and optimization of hybrid plasmonic waveguide as a platform for biosensing," *IEEE Photon. J.*, vol. 6, no. 4, pp. 1 – 10, Aug. 2014.

[21] J. Homla, S. S. Yee, and G. Gauglitz, "Surface plasmon resonance sensors: review," *Sens. Actuators B, Chem.*, vol. 54, no. 1, pp. 3 – 15, Jan. 1999.

[22] S. Ghosh and B. M. A. Rahman, "Full vectorial finite element modelling: a composite plasmonic horizontal slot waveguide as a bio-sensor," *13th International Conference on Fiber Optics and Photonics*, https://doi.org/10.1364/PHOTONICS.2016.Tu5C.3

[23] B. M. A. Rahman and J. B. Davies, "Finite-element solution of integrated optical waveguides," *J. Lightw. Technol.*, vol. 2, no. 5, pp. 682-688, Oct. 1984.

[24] J.-M. Jin, *The Finite Element Method in Electromagnetics*, 3rd ed. Hoboken, Nj, USA: Wiley, 2014.

[25] S. Ghosh and B. M. A. Rahman, "An innovative straight resonator incorporating a vertical slot as an efficient bio-chemical sensor," *Journal of Selected Topics in Quantum Electronics*, vol. 23, no. 2, pp. 1-8, Mar. 2017.

[26] A. D. Berk, "Variational principles for electromagnetic resonators and waveguides," *IRE Trans. Antennas Propag*., vol.4, pp. 104 – 111, Apr. 1956.
[27] B. M. A. Rahman and J. B. Davies, "Penalty function improvement of waveguide solution by finite element," *IEEE Trans. Microw. Theory Techn*., vol. 32, no. 8, pp. 922 – 928, Aug. 1984.
[28] W. Wang, Y. Tian, X. Wang, H. He, Y. Xu, C. He, and X. Li, "Ethanol sensing properties of porous ZnO spheres via hydrothermal route," *J. Mater. Sci.*, vol. 48, pp. 3232 – 3238, 2013.
[29] L. Zhang, J. Zhao, H. Lu, L. Li, J. Zheng, H. Li and Z. Zhu, "Facile synthesis and ultrahigh ethanol response of hierarchically porous ZnO nanoplates," *Sens. Actuators B, Chem.*, vol. 54, no. 1, pp. 3 – 15, Jan. 1999.
[30] Z. Jiang and J. Zhan, "Fabrication and gas-sensing properties of porous-ZnO nanoplates," *Advanced Materials*, vol. 161, no. 1, pp. 209 - 215, 2012.
[31] A. Garahan, L. Pilon, J. Yin, and I. Saxena, "Effective optical properties of absorbing nanoporous and nanocomposite thin films," *J. Appl. Phys.*, vol. 101, no. 1, pp. 014320, 2007.
[32] W. L. Bond, "Measurement of the refractive indices of several crystals," *J. Appl. Phys.*, vol. 36, no. 5, pp. 1674-1677, 1965.
[33] S. Kedenburg, M. Vieweg, T. Gissibl, and H. Giessen, "Linear refractive index and absorption measurements of nonlinear optical liquids in the visible and near-infrared spectral region," *Opt. Mater. Express*., vol. 2, no. 11, pp. 1588-1611, Oct. 2012.
[34] S. Babar and J. H. Weaver, "Optical constants of Cu, Ag and Au revisited," Appl. Opt., vol. 54, no. 3, pp. 477 – 481, Jan. 2015.
[35] H. H. Li, "Refractive index of silicon and germanium and its wavelength and temperature derivatives," *J. Phys. Chem. Ref. Data*, vol. 9, no. 3, pp. 561 – 658, 1980.
[36] P. Berini, "Bulk and surface sensitivities of surface plasmon waveguides," New J. Phys. Vol. 10, no. 10, pp. 1 – 37, 2008.
[37] P. Lommens, D. V. Thourhout, P. F. Smet, D. Poelman, and Z. Hens, "Electrophoretic deposition of ZnO nanoparticles: from micropatterns to substrate coverage," *Nanotechnology*, vol. 19, no. 24, pp. 245301, 2008.

Souvik Ghosh was born in Kolkata, India. He received his B.Tech and M.Tech degree in Optics and Optoelectronics (First class, 1st rank) from Calcutta University (C.U), India in 2012 and 2014, respectively. He is currently pursuing Ph.D. degree at the School of Mathematics, Computer Science and Engineering, City, University of London, U.K. He is also a recipient of Erasmus Mundus AREAS+ Ph.D. fellowship.

His research interests include the application of two dimensional and three dimensional finite element method in photonic devices, waveguides as well as resonators. Currently he is working on the development and application of finite element method for simulation of complex plasmonic waveguides and resonators.

B. M. A. Rahman (S'80–M'82–SM'93–F'2016) received the B.Sc.Eng and M.Sc.Eng. degrees in electrical engineering with distinctions from Bangladesh University of Engineering and Technology (BUET), Dhaka, Bangladesh, in 1976 and 1979, respectively, and the Ph.D. degree in Electronics from the University College London, London, U.K., in 1982.

From 1976 to 1979, he was a Lecturer with the Electrical Engineering Department, BUET. In 1982, he was with the University College London as a Postdoctoral Research Fellow and continued his research work on the development of finite-element method for characterizing optical guided-wave devices. In 1988, he joined City, University of London, as a Lecturer, and became a Full Professor in 2000. At City University, he leads the research group on photonics modeling, specializing in the use of rigorous and full-vectorial numerical approaches to design, analyze, and optimize a wide range of photonic devices, such as spot-size converters, high-speed optical modulators, power and polarization splitters, photonic crystal fibers, terahertz waveguides, etc. He has published more than 500 journals and conference papers, and his journal papers have been cited more than 4200 times. He has supervised more than 26 completed PhD students as their first supervisor and received more than $10 M research grants.

Prof. Rahman is a Fellow of the IEEE, the Optical Society of America, and the SPIE.